

Crystallization and Microstructure of Yttria-Stabilized-Zirconia Thin Films Deposited by Spray Pyrolysis

Barbara Scherrer,* Sebastian Heiroth, Regina Hafner, Julia Martynczuk, Anja Bieberle-Hütter, Jennifer L. M. Rupp, and Ludwig J. Gauckler

The crystallization and microstructural evolution upon thermal treatment of yttria-stabilized zirconia (YSZ, $Zr_{0.85}Y_{0.15}O_{1-\delta}$) thin films deposited by spray pyrolysis at 370 °C are investigated. The as-deposited YSZ films are mainly amorphous with a few crystallites of 3 nm in diameter and crystallize in the temperature range from 400 °C to 900 °C. Fully crystalline YSZ thin films are obtained after heating to 900 °C or by isothermal dwells for at least 17 h at a temperature as low as 600 °C. Three exothermic heat releasing processes with activation energies are assigned to the crystallization and the oxidation of residuals from the precursor. Microporosity develops during crystallization and mass loss. During crystallization the microstrain decreases from 4% to less than 1%. Simultaneously, the average grain size increases from 3 nm to 10 nm. The tetragonal phase content of the YSZ thin film increases with increasing temperature and isothermal dwell time. Based on these data, gentle processing conditions can be designed for zirconia based thin films, which meet the requirements for Si-based microfabrication of miniaturized electrochemical devices such as micro-solid oxide fuel cells or sensors.

1. Introduction

Integration of metal oxide thin films into micro-electromechanical systems (MEMS) allows the miniaturization of sensors, energy converters, electromechanical, chemical, and optical devices.^[1–6] Processing of such new units is challenging since MEMS are usually based on Si microfabrication at low temperatures (typically below 250 °C) whereas metal oxide thin films are processed at high temperatures (typically above 500 °C). Therefore, either high temperature MEMS are required or gentle processing routes at low temperature have to be established for metal oxide thin films. Thereby, thermal degradation by interdiffusion or interfacial reactions as well as processing induced stresses can be minimized.^[7,8]

B. Scherrer, R. Hafner, J. Martynczuk, A. Bieberle-Hütter, J. L. M. Rupp, L. J. Gauckler
Nonmetallic Inorganic Materials
ETH Zurich, Wolfgang-Pauli-Str.10, CH-8093 Zurich, Switzerland
E-mail: barbara.scherrer@mat.ethz.ch
S. Heiroth
General Energy Research Department
Paul Scherrer Institut
CH-5232 Villigen-PSI, Switzerland

DOI: 10.1002/adfm.201101268

Micro-solid oxide fuel cells are seen to replace conventional batteries in portable electrical devices and are produced by microfabrication. For micro-solid oxide fuel cell membranes, yttria-stabilized zirconia (YSZ) thin films with high oxygen conductivity at low temperature (<600 °C) are needed.^[6] The total conductivity of YSZ thin films deposited on sapphire spreads over almost 3 orders of magnitude at 500 °C in the literature.^[9–16] Currently, the effect of microstructural features, such as the grain size, degree of crystallinity, strain, and crystal symmetry on the electrical transport properties is investigated in order to understand the large scatter in the conductivity data. Therefore the knowledge of crystallization and microstructural features is important and needs to be studied in detail for thin films. This knowledge will then help to optimize the YSZ thin film for its use in micro-solid oxide fuel cells.

Precipitation-based thin films are one option to combine gentle processing conditions with various microstructural features. With precipitation-based deposition methods like spray pyrolysis, spin-coating or sol-gel, thin films are amorphous after deposition and can be crystallized by subsequent annealing.^[9,17–19] The crystallization behavior of YSZ is described in the literature for powders fabricated by precipitation-based techniques;^[20–23] no details are known about the crystallization behavior of precipitation-based thin films. The phase change from amorphous to crystalline YSZ powder occurs between 320 °C and 600 °C. The crystallization activation energy ranges from 119 kJ mol⁻¹ to 337 kJ mol⁻¹.^[20–23] The large scatter in activation energy is partly related to different amounts of yttria, but also to different chemistries of the precursors used in the precipitation process.

Crystal symmetry is an important microstructural parameter. Yashima et al. studied the phase diagram for yttria doped zirconia in detail.^[24] It shows that 8 mol% yttria stabilized zirconia is cubic at high temperatures (>1300 °C); nevertheless, during cooling, the symmetry changes to a tetragonal symmetry, the so-called t'' or even t' symmetries. Both exhibit an oxygen ion displacement along the c -axis, but the former has an axial ratio $c/a = 1$, whereas the second has a slightly elongated c -axis. The metastable t'' symmetry with the displacement of the oxygen ions is only very weakly reflected in

the conventional X-ray diffraction pattern, but can be probed effectively by Raman spectroscopy.^[25] The few data on crystal symmetry of YSZ thin films in the literature show that the crystal symmetry strongly depends on the deposition and processing conditions.^[26–29]

Strain is another important property of a thin film. Different types of strain are present in thin films. With X-ray diffraction (XRD), two different strains can be measured, the lattice strain and the microstrain. The lattice strain originates from the thermal mismatch between substrate and thin film and results in a peak shift due to a compressed or stretched lattice of the thin film, whereas the microstrain manifests in a broadening of the XRD peaks and reflects the defect density of the structures. The microstrain is not oriented and averages out over the thin film. Recently, research on strain in thin films increased, mainly due to the eight orders of magnitude higher electrical conductivity measured in heavily strained thin YSZ layers embedded in a multilayer structure.^[30] Besides this study, others found only half an order of magnitude higher conductivity for YSZ heterolayers.^[31–33] Results from the strain state modeling predict higher oxygen ion diffusivity within the (100) direction of YSZ, whereby the maximal increase is almost four orders of magnitude at 4% tensile strain.^[34,35] At higher strains, the Zr–O bond strengthens again, which leads to an increased migration barrier.^[34,35] The high electrical conductivity may also be related to the amount of interfaces which increase the number of mobile charge carriers.^[36] For single-layered YSZ thin films, an increased electrical conductivity due to strain is not reported so far. Microstrains of about 2% and lower than 0.4% are reported for sputtered and PLD YSZ thin films.^[28,37] For thin films produced by wet processing, only microstrain data on gadolinia doped ceria is available. The measured microstrains are about one order of magnitude higher than those reported on pulsed laser deposited YSZ thin films.^[38]

In this paper, a systematic study on the crystallization behavior of $Zr_{0.85}Y_{0.15}O_{1-\delta}$ thin films deposited by spray pyrolysis from the wet state and its grain size, microstrain and crystal symmetry evolution are presented. The experimental results are discussed with respect to microstructural engineering and integration of these films as electrolytes in micro-solid oxide fuel cells.

2. Experimental Section

2.1. Thin Film Preparation

YSZ thin films were deposited by air-blast spray pyrolysis; details on this method have been previously published.^[18,39] The precursor solution was pumped to a spray gun (Compact 2000KM, Böllhoff Verfahrenstechnik) where it was atomized with 1 bar air pressure and sprayed on a heated substrate at 370 ± 5 °C. The spray pyrolysis precursor solution consisted of zirconium acetylacetonate (Alfa Aesar, 99% purity) and yttrium chloride hydrate (Alfa Aesar, 99.9% purity) dissolved in 80 vol% tetraethylene glycol (Aldrich, 99%), 10 vol% polyethylenglycole 600 (Fluka) and 10 vol% ethanol (Fluka, 99.9%). The total salt concentration was 0.05 mol L⁻¹. A molar ratio of Zr:Y = 85.2 :14.8

was chosen to obtain a 8 mol% yttria-stabilized zirconia (YSZ, $Zr_{0.852}Y_{0.148}O_{2-\delta}$) film composition.^[8] The liquid flow rate for thin films was 2.5 mL h⁻¹ during deposition whereas powders for the differential scanning calorimetry (DSC) and Raman measurements were sprayed with a liquid flow rate of 50 mL h⁻¹. The obtained powders were held at 370 °C for 5 h after deposition to account for the faster deposition rate compared to the slower flow rate used for the thin films. As a substrate, randomly orientated sapphire single crystals (Stettler) were used. The working distance between the spray nozzle and the hot plate was kept at 39 cm during all experiments. Spray time was 100 min and 10 h for the YSZ thin films and powders, respectively. The YSZ was subsequently annealed at 400 °C, 600 °C, 800 °C and 1000 °C in air with an isothermal hold of 20 h and a heating and cooling rate of 3 °C min⁻¹ or air-quenched after reaching the desired annealing temperature.

2.2. Microstructure and Phase Analysis

Top-view microstructures of the thin films were characterized by scanning electron microscopy (SEM, Zeiss LEO Gemini 1530) with an in-lens detector. Prior to imaging, the thin films were coated with carbon in order to avoid charging and to allow imaging at higher resolutions.

The thickness and cross-section microstructure of YSZ thin films were investigated by transmission electron microscopy (TEM). TEM lamellae of an as-deposited YSZ thin film on sapphire and a thin film annealed at 600 °C for 20 h were prepared by focused ion beam (FIB) technique. Both thin films were coated with platinum in order to avoid charging. A CrossBeam NVision 40 from Carl Zeiss with a gallium liquid metal ion source, a gas injection system and a micromanipulator MM3A from Kleindiek was used. After electron beam deposition of carbon in SEM mode at low scan speeds, thin films were protected by a carbon cap and trenches were milled from 13 nA down to 10 pA at 30 kV. TEM lamellae were cut free with trenches from both sides with 13 nA and 3 nA at 30 kV. After the lift-out was performed, the lamellae were polished to ion transparency with currents down to 10 pA at 30 kV. The amorphization was diminished by low kV showering for several seconds at 5 kV and 2 kV. A FEI Tecnai F-30 (field emission gun) transmission electron microscope with an accelerating voltage of 300 kV and post-column CCD camera was used to obtain bright-field and high-resolution transmission electron microscopy (BFTEM and HRTEM) images and selected area electron diffraction (SAED) patterns. In particular, the as-deposited sample was treated with utmost care, as amorphous spray pyrolyzed YSZ thin films tend to crystallize in the electron beam which was already visible in the SAED and HRTEM after exposure to the 300 kV beam for some minutes. The shown images were acquired at a new position of the TEM lamella after the adjustments were done elsewhere.

Crystallization behavior of amorphous spray pyrolysis YSZ was investigated by differential scanning calorimetry and thermogravimetry (DSC/TG, Netzsch STA 449C). The instrument was calibrated with calibration standards (Netzsch 6.223.5-91.2).

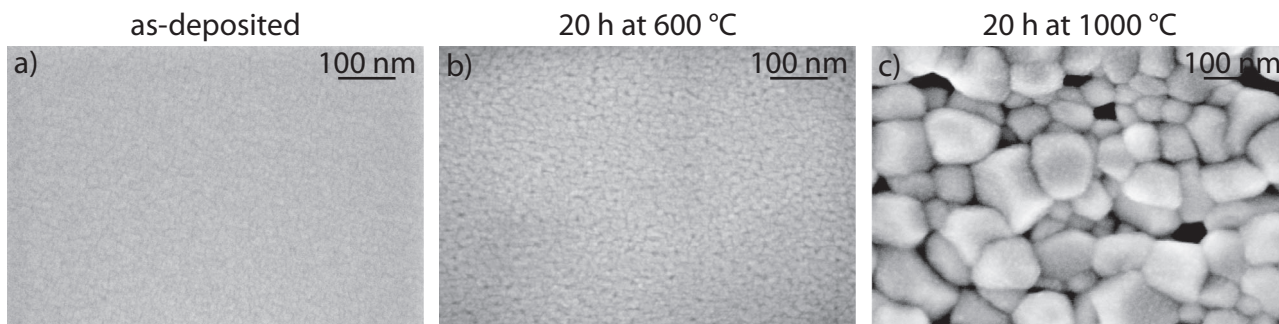


Figure 1. SEM top-view microscopy images of YSZ thin films deposited by spray pyrolysis after different thermal treatment: a) as-deposited, b) 600 °C for 20 h and c) 1000 °C for 20 h. The heating and cooling rates were 3 °C min⁻¹.

As-deposited amorphous YSZ was scratched off from the sapphire substrate and the powder obtained as such was measured in DSC up to 1300 °C at 3 °C min⁻¹. The powder was always enclosed in a Pt crucible with a lid and measured against an empty Pt crucible with a lid as a reference under static air atmosphere. A subsequent correction measurement was performed for quantitative DSC analysis using a fully crystallized (at 1300 °C) YSZ spray pyrolysis powder of the same mass and at equivalent experimental conditions. The crystallinity was calculated from the ratio of the proceeded to the complete enthalpy. A mass spectrometer (QMS422, Pfeiffer) was coupled to the DSC/TG to analyze the emerging gases. During this measurement, an artificial air gas flow of 60 sccm consisting of Ar and O₂ was used.

The YSZ thin films were analyzed with X-ray diffraction (XRD, PANalytical X'pert). The setup was equipped with a copper radiation source operated at 45 kV and 40 mA with parallel beam geometry. The average grain size and microstrain were determined by fitting the diffraction patterns with the open-source FullProf suite program (2.00).^[40] The instrumental broadening was corrected using a sintered microcrystalline 8 mol% YSZ pellet as a reference for the strain-free state. For average grain sizes in the films larger than 80 nm, the intercept lengths of grain sizes from SEM pictures with more than 300 grains were measured with Lince 2.4.2 β software (Technische Universität Darmstadt, Germany).

Additional information about the crystal symmetry was derived by Raman spectroscopy employing a Raman microscope (LabRAM Series, Horiba Jobin Yvon) with a He-Ne excitation laser (λ : 632.8 nm, output power: ~10 mW). For Raman analysis, *ex situ* annealed, scratched off YSZ powder deposited on sapphire as described above was selected. The Raman spectra were fitted with Voigt functions to derive the peak position and full width at half maximum (FWHM).

3. Results and Discussion

Two kinds of thermal treatments were investigated in this study: i) air-quenching in which the samples were removed from the furnace after reaching the desired annealing temperatures, and ii) samples annealed with an isothermal dwell for 20 h.

3.1. Microstructure

The microstructural properties of the YSZ thin films were analyzed as a function of isothermal annealing. In **Figure 1**, a SEM top-view of an as-deposited spray pyrolyzed YSZ thin film and thin films after isothermal annealing at 600 °C for 20 h and 1000 °C for 20 h are shown. All YSZ thin films were crack-free after deposition as well as after annealing and had a thickness of 300 nm to 800 nm. Exemplarily, two YSZ thin film cross-sections are shown in **Figure 2** (a: as-deposited and b: annealed at 600 °C for 20 h). As-deposited films have a uniform appearance with no visible grains according to SEM analysis (Figure 1a). The fine structure visible in the top-views of the film is due to the sample preparation for SEM. According to high-resolution TEM (Figure 2c) and XRD (discussed in section 3.3), a few crystallites with an average diameter of about 3 nm are present within the amorphous matrix. Crystallization and crystal growth was observed during TEM analysis. Therefore the shown images were acquired at a new position of the thin film after the adjustments were done elsewhere. After annealing at 600 °C for 20 h (Figure 1b and Figure 2b), fine grains with an average grain size of 6 nm, deduced from peak broadening of the X-ray diffraction pattern using the Scherrer equation and confirmed by TEM, are formed. The selected area electron diffraction (SAED) patterns (Figure 2d) of an as-deposited YSZ thin film on the left-hand side and a YSZ thin film annealed at 600 °C for 20 h on the right-hand side are shown. The pattern for the as-deposited film consists of several undefined rings hinting at a cubic YSZ lattice. This is interpreted as a high degree of amorphous phase along with some crystalline material. For the annealed film, in contrast, the ring-shaped pattern is composed of discrete reflections due to the nanocrystallinity. Both films are cubic and there is no evidence for a tetragonal phase which would be indicated by an additional ring between the (200) and the (220) ring due to the (102) lattice planes of the tetragonal phase.^[42] The sample annealed at 1000 °C for 20 h exhibits coarse grains with an average grain size of 130 \pm 50 nm (Figure 1c). Intergranular pores are visible in both samples after isothermal annealing (Figure 1b and c). These pores are likely due to out-gassing of residual organics, similar to films made by spin-coating and spray pyrolysis.^[8,42,43] The microstructure of the air-quenched YSZ thin films is

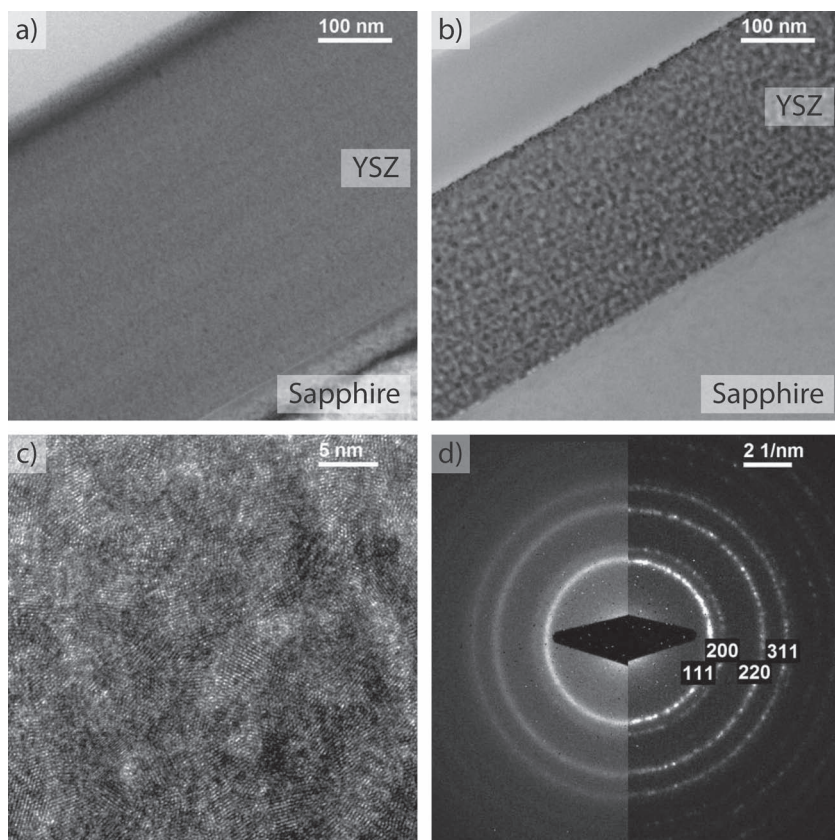


Figure 2. Bright-field TEM cross-sections of a) an as-deposited and b) a YSZ thin film annealed at 600 °C for 20 h, which were produced by spray pyrolysis on sapphire, c) HRTEM micrograph of the as-deposited YSZ thin film and d) the SAED patterns of both YSZ thin films, left: as-deposited and right: annealed at 600 °C for 20 h.

similar to the ones with 20 h dwell, but with different grain sizes. The average grain sizes are listed in **Table 1** and are discussed in section 3.3.

3.2. Crystallization

DSC/TG measurements combined with mass spectrometry were performed to analyze the crystallization behavior during heating in more detail. In **Figure 3** and **Figure 4**, the temperature dependencies of the mass loss, the enthalpy evolution, and the gas evolution are shown. Up to the deposition temperature of 370 °C an endothermic DSC peak is accompanied by a mass loss of 3 wt% (**Figure 3**) which is assigned to the desorption of water (m/z 18) and some carbon dioxide (m/z 44) according to mass spectrometry (**Figure 4**). Above 370 °C, three exothermic DSC signals (designated as 1–3 in **Figure 3**) are detected and attributed to the crystallization and oxidation of residuals from the precursor of the amorphous thin film. These exothermic signals are accompanied by a mass loss of 2.4 wt%, assigned by mass spectrometry to carbon dioxide resulting from organic residuals (**Figure 4b**). The crystallization is finished at 900 °C since no enthalpy change was detected at higher temperatures. An additional mass loss of 2.2 wt% was still observed in the temperature interval between 900 °C and 1300 °C due to

further release of carbon dioxide (**Figure 4b**). In order to further investigate the crystallization kinetics, DSC measurements at different heating rates were performed (**Figure 5a**). Three exothermic processes at different peak temperatures (T_{C1} , T_{C2} and T_{C3}) were observed between 400 °C and 900 °C. From the enthalpy and the three peak temperatures the activation energies were calculated to 125.5 kJ mol⁻¹, 285.7 kJ mol⁻¹ and 84.9 kJ mol⁻¹ according to the Kissinger equation (**Figure 5b**).^[44] The peak temperature of the first reaction is at 460 °C and corresponds to the crystallization reported in literature for YSZ crystallization, which is between 320 °C and 540 °C with activation energies between 119 kJ mol⁻¹ and 327 kJ mol⁻¹.^[20–23,45,46] The two other peak temperatures measured in this study are higher than 700 °C. No gas or mass changes were detected for the second reaction, whereas during the first and third reaction water and carbon dioxide are released. The third process is supposedly due to the oxidation of residuals from the precursor. Obviously the crystallization of spray pyrolyzed YSZ films is accompanied by a release of water and carbon dioxide, which were incorporated in the as-deposited amorphous material. This finding is in perfect agreement with those obtained for the crystallization of spray pyrolyzed ceria thin films.^[47] In **Figure 6**, the enthalpy evolution at 600 °C for an isothermal dwell is shown. The exothermal enthalpy evolution decreases rapidly and turns almost zero after 100 min at 600 °C. No enthalpy change could be measured after 1000 min indicating that the film is then fully crystallized.

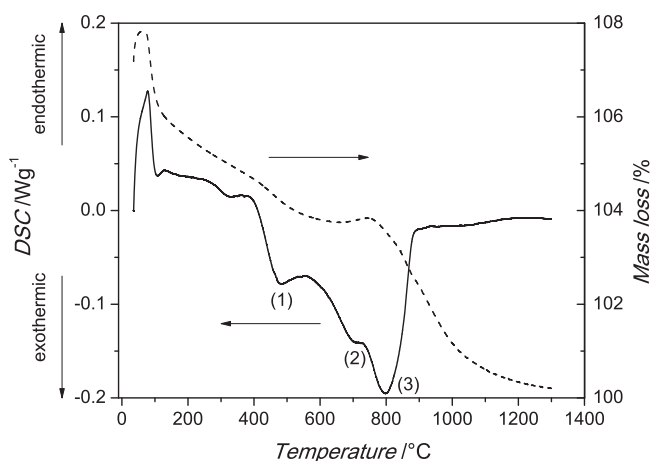
We conclude that crystallization of spray pyrolyzed YSZ is finished when samples are heated up to 900 °C or after an isothermal dwell at 600 °C for at least 1000 min (~17 h). The three distinct processes identified in DSC and TG analysis in this study differ clearly from the one-step crystallization observed for precipitated powders, which shows that the solvents used in the spray pyrolysis process as well as the processing itself have a strong influence on the crystallization behavior of YSZ.^[20–23] It can be concluded that the activation energy of the crystallization varies with the solvents used for processing and is not only material specific.

3.3. Grain Growth and Microstrain

Figure 7 shows X-ray diffraction patterns for spray pyrolyzed YSZ films, annealed at different temperatures for different durations. All XRD patterns match unambiguously with the cubic fluorite-type phase of zirconia. No tetragonal splitting or additional reflections can be observed. **Figure 7a** shows the diffractogram with broad reflections of the as-deposited film and those after annealing at higher temperatures with

Table 1. Raman shifts, FWHM, intensity ratio of the peak fitting for the double peak at about 629 cm^{-1} , microstrain, average grain sizes and crystallinity of YSZ with respect to their annealing conditions.

Annealing conditions	Raman shift [cm^{-1}]	Raman FWHM [cm^{-1}]	I_4/I_5	Microstrain [%]	Grain size [nm]	Crystallinity [%]
air-quenched						
0 h at 600 °C	—	—	—	1.0 ± 0.1	5 ± 5	27
0 h at 800 °C	259.3	32.0	0.45	0.8 ± 0.1	10 ± 5	85
	345.6	42.1				
	492.7	17.3				
	628.8	53.3				
	709.1	21.5				
0 h at 1000 °C	261.1	39.9	0.40	—	—	100
	350.5	48.2				
	479.6	29.7				
	631.1	50.2				
	710.6	22.6				
isothermal dwell for 20 h						
20 h at 600 °C	261.1	37.4	0.57	0.9 ± 0.2	9 ± 5	100
	345.1	38.9				
	493.8	17.9				
	627.3	53.1				
	709.3	20.8				
20 h at 800 °C	254.9	44.6	0.42	0.6 ± 0.1	13 ± 7	100
	351.6	45.5				
	474.3	32.7				
	630.1	49.9				
	710.0	30.1				
20 h at 1000 °C	264.0	33.0	0.35	0.4 ± 0.2	130 ± 50	100
	338.1	36.5				
	473.4	27.6				
	631.1	55.1				
	710.0	43.4				

**Figure 3.** Enthalpy evolution and mass loss of as-deposited YSZ powder produced by spray pyrolysis measured in dynamic air at 10 °C min^{-1} .

sharp peaks. Comparing the XRD patterns to the isothermally annealed thin films (Figure 7b), a continuous sharpening of the peaks is found with increasing temperature. In Figure 8, the evolutions of the average grain size and microstrain are shown for air-quenched samples heated at 3 °C min^{-1} (a), and after an isothermal dwell for 20 h (b). As-deposited thin films have a microstrain of 4% and grains with an average size of about 3 nm, which are embedded in an amorphous matrix as confirmed by TEM microscopy images (Figure 2c and Figure 8a). Microstrain decreases with further annealing which reflects the healing of defects. Simultaneously, grain growth occurs. Grain growth stagnation is observed (not shown), as reported for ceria thin films previously.^[48] Please note the rather high residual microstrain of 0.9% after 20 h at 600 °C and 0.4% after 20 h at 1000 °C in these YSZ films, respectively. These microstrain values indicate a high defect density. Lower microstrain and larger grain sizes are reported for YSZ thin films obtained by pulsed laser deposition in

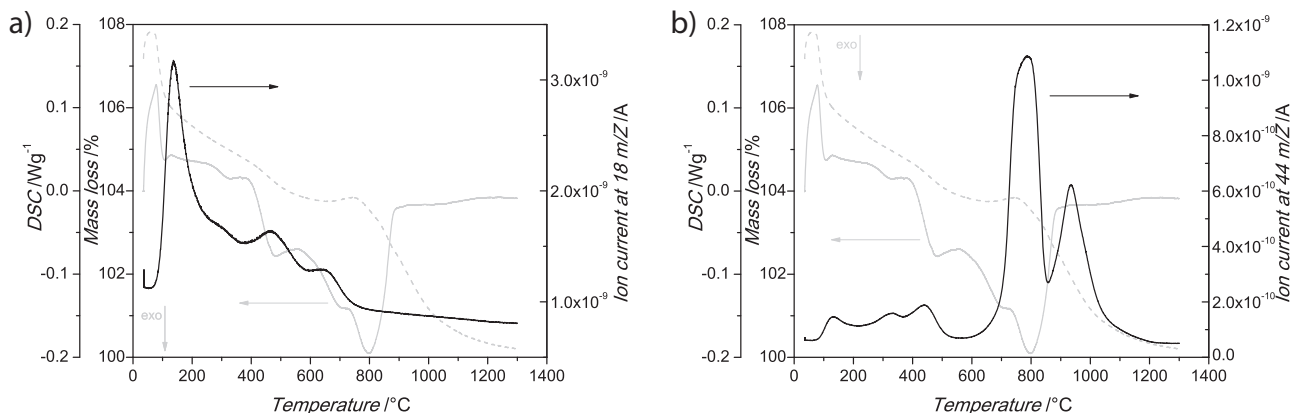


Figure 4. Mass spectrometry data of gas evolution of as-deposited YSZ powder produced by spray pyrolysis during heating in dynamic air at 10 °C min^{-1} . Mass-to-charge ratios are plotted a) at 18 and b) 44.

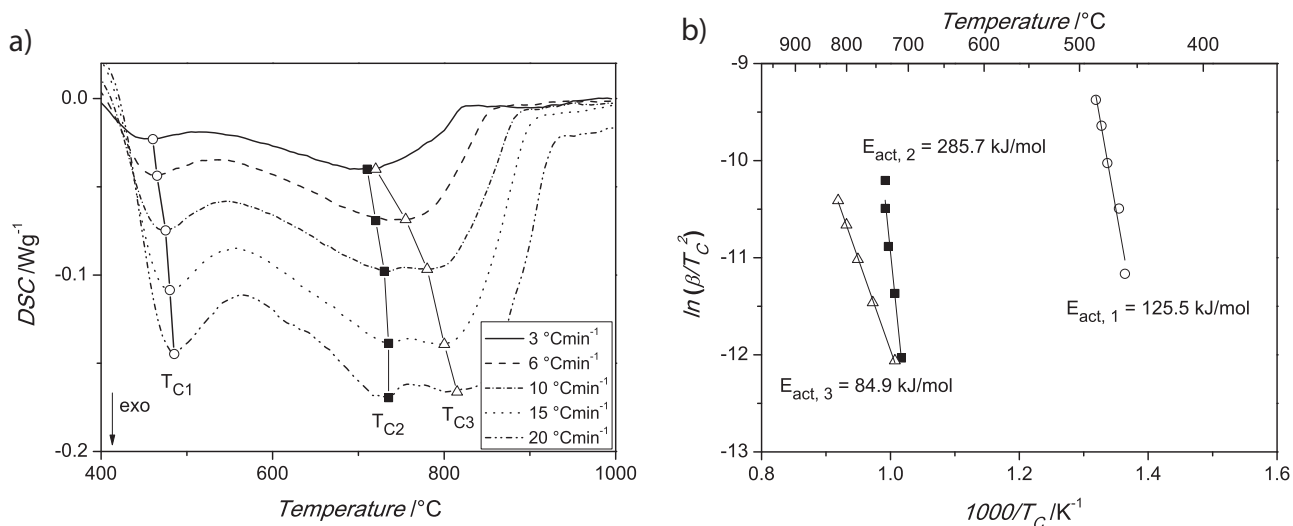


Figure 5. Non-isothermal crystallization during heating of YSZ powder produced by spray pyrolysis in static air: a) exothermic DSC heat release for different heating rates between 400 °C and 1000 °C . b) Kissinger plot for YSZ produced by spray pyrolysis. Crystallization peak temperature is denoted as T_C and heating rate as β .

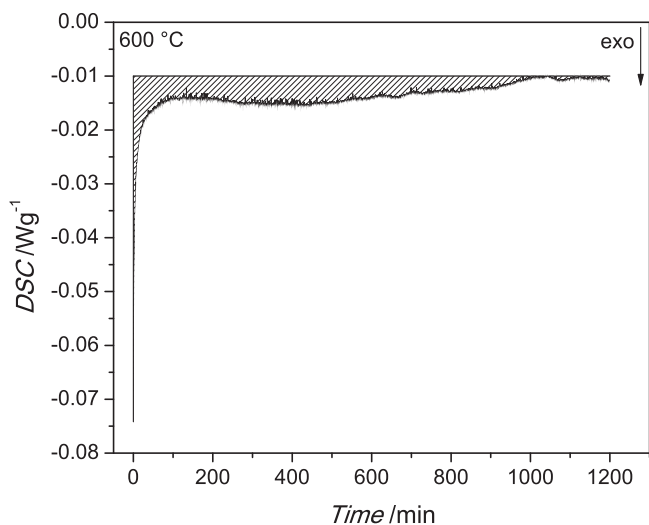


Figure 6. Isothermal enthalpy evolution at 600 °C of YSZ powder produced by spray pyrolysis measured in static air.

literature.^[28,37,49] The higher defect density of the spray pyrolysis YSZ compared to the pulsed laser deposited thin films is most likely caused by the residual organics.

3.4. Crystal Symmetry

In **Figure 9**, Raman spectra of YSZ powders deposited by spray pyrolysis are shown. No data could be obtained for air-quenched YSZ at 600 °C due to fluorescence of residual organics (**Figure 9a**). Raman modes at $431.8 \pm 0.2\text{ cm}^{-1}$ and $453.5 \pm 0.4\text{ cm}^{-1}$ are due to aluminum oxide particles from the crucibles used during annealing and are denoted with an asterisk in the plot. In all the spectra, six Raman peaks numbered from 1 to 6 are visible. The Raman shifts and FWHM are summarized in **Table 1**. According to the literature, the Raman spectra for the cubic phase exhibit a single peak at 617 cm^{-1} which is attributed to the O–Zr–O stretching mode in F_{2g} symmetry.^[50] A displacement of the oxygen ions along the [100] direction results in a transition from cubic to tetragonal symmetry.^[25,51]

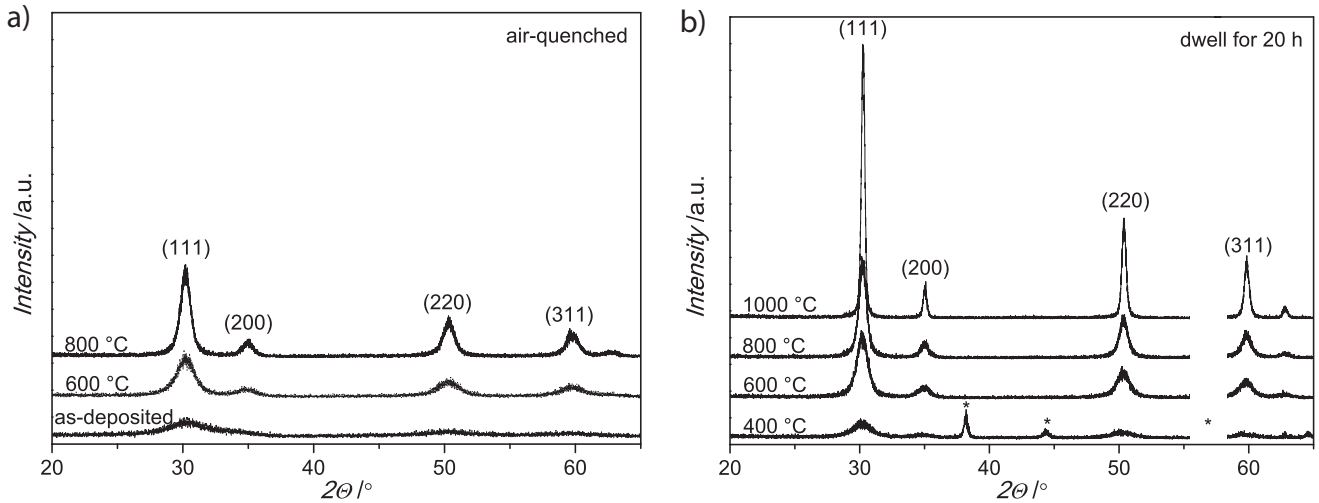


Figure 7. X-ray diffraction pattern of YSZ thin films deposited by spray pyrolysis with respect to their annealing conditions: a) air-quenched at different temperatures, b) after isothermal dwell for 20 h at different temperatures with heating and cooling at 3 °C min^{-1} . The intensity scale is identical for both diagrams. Sapphire substrate reflections are denoted with an asterisk (*).

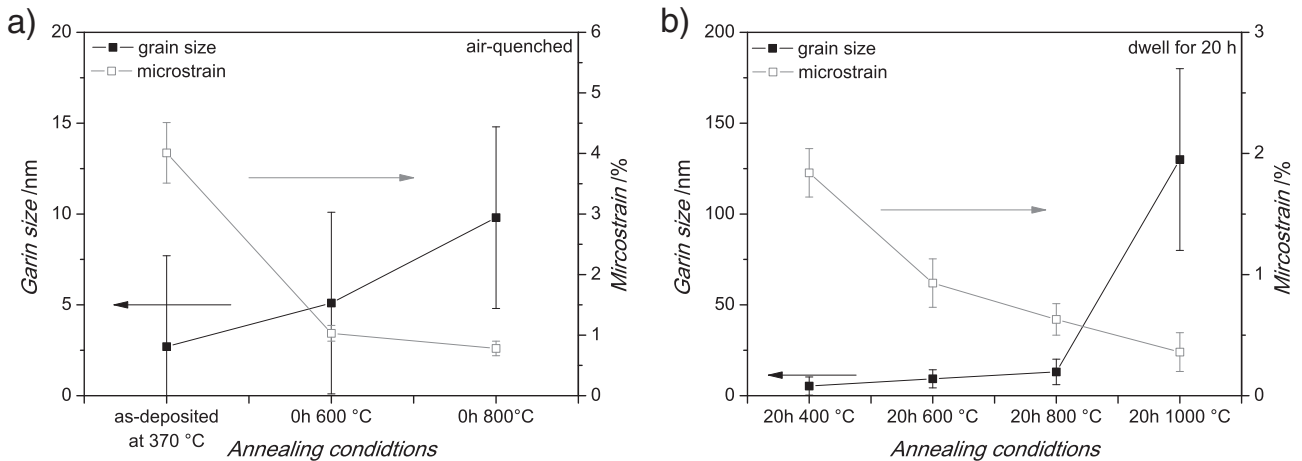


Figure 8. Grain size and microstrain of YSZ thin films with respect to their annealing conditions: a) air-quenched at different temperatures, b) after isothermal dwell for 20 h at different temperatures with heating and cooling at 3 °C min^{-1} .

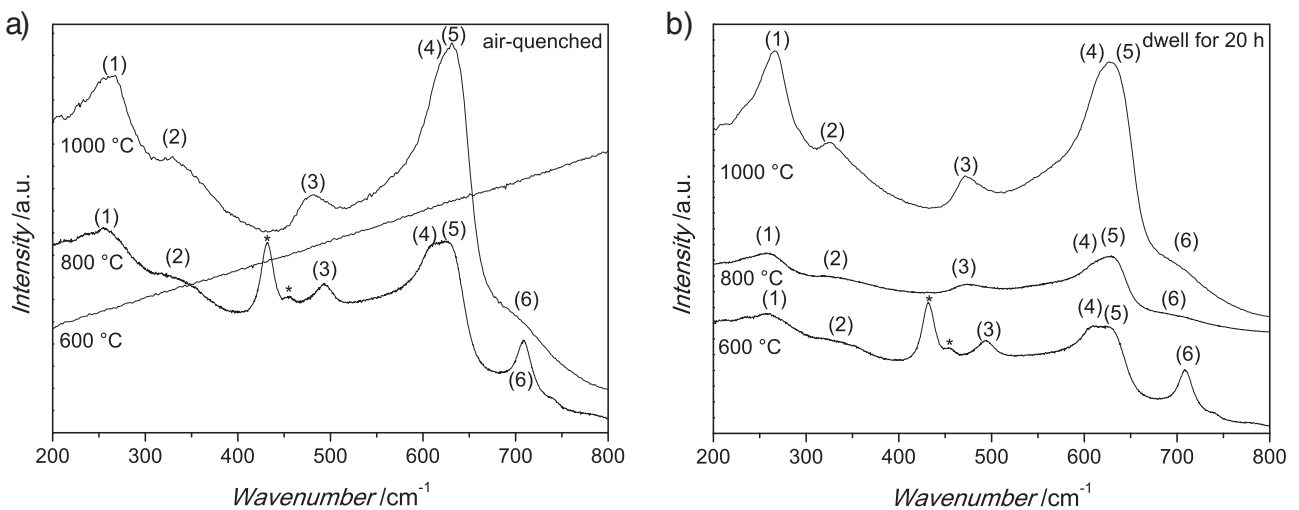


Figure 9. Raman spectra of YSZ powders deposited by spray pyrolysis with respect to their annealing conditions: a) air-quenched at different temperatures, b) after isothermal dwell for 20 h at different temperatures with heating and cooling at 3 °C min^{-1} . Sapphire substrate reflections are denoted with an asterisk (*).

Tetragonal zirconia exhibits 6 Raman modes due to its lower symmetry according to the literature.^[52] The assignment of the frequencies to the symmetry is still under discussion.^[51–55] The first tetragonal peak at around 130 cm^{-1} was not measured due to the low wavenumber. In literature, the tetragonal peaks at around 130 cm^{-1} , 474 cm^{-1} and 647 cm^{-1} were mostly assigned to the E_g symmetry, whereas the peaks at around 260 cm^{-1} , 346 cm^{-1} and 600 cm^{-1} were attributed to an A_{1g} or B_{1g} symmetry.^[51–55] The peaks 1, 2, 3 and 5 belong to the tetragonal symmetry, whereas peak 4 to the cubic one (Figure 9). Peak 6 may be allocated to the oxygen ion hopping.^[56–58] The relative peak intensity for this mode decreases with increasing annealing temperature and dwell time. In this study, all samples annealed at temperatures higher than 600 °C or with isothermal dwells for 20 h show a tetragonal and cubic phase mixture according to Raman spectroscopy (Figure 9). The Raman modes 1 and 2 scatter around $260 \pm 3\text{ cm}^{-1}$ (peak 1) and $346 \pm 5\text{ cm}^{-1}$ (peak 1), respectively, and show no dependency on the annealing conditions. Whereby the former is reported to be very sensitive to a t–c transition and should show a blue shift.^[51–53] A red shift was observed for the E_g mode from 493 cm^{-1} to 474 cm^{-1} (peak 3) with increasing annealing temperature and time. Such a shift is related to an increased tetragonal symmetry.^[51–53] Between 500 cm^{-1} and 680 cm^{-1} , a superposition of two tetragonal modes and the cubic mode is present (peak 4 and 5). The tetragonal peak at around 600 cm^{-1} has a low intensity, and therefore, the measured peak 4 is mostly due to the cubic phase within the YSZ thin film. A systematic blue shift was observed for this superposition from 627.2 cm^{-1} to 631.5 cm^{-1} for increasing temperature and dwell time. Additionally, the peak's asymmetry increases. The shift and the asymmetry indicate that the tetragonal phase content increases with increasing annealing temperature and time. This is supported by the intensity ratio of the mode at lower (peak 4, cubic) over the one at higher frequency (peak 5, tetragonal), which becomes lower with increasing temperature (Table 1). This means that the intensity of the second peak (peak 5) increases, which indicates a higher content of tetragonal symmetry. An increasing tetragonal phase content with increasing temperature was also found in pulsed laser deposited YSZ thin films.^[28] A transition from a metastable crystal symmetry to the thermodynamically more stable crystal structure with increasing temperature and time is commonly observed for ceramic powders and thin films synthesized in the amorphous state and crystallized at very low temperatures.^[46,59–63]

With Raman scattering experiments, a mixture of tetragonal and cubic crystal symmetry was measured whereas with X-ray and electron diffraction, the YSZ thin films were cubic. This leads to the conclusion that the cations form a cubic lattice due to the fact that with X-ray and electron diffraction, mainly the relatively heavy cations are probed, whereas Raman spectroscopy probes the bond strength. The oxygen anions are displaced along the [100] direction and transform the cubic lattice of the cations in a tetragonal lattice. This so-called t \bar{c} crystal structure is described by Yashima et al.^[24] In bulk YSZ, coherent microdomains of 1–10 nm in size with t \bar{c} symmetry embedded in a cubic matrix were observed and correlated with a decrease in ionic conductivity.^[64–66] These microdomains show a Y depletion similar to the ones found in calcium-stabilized zirconia reported earlier.^[67,68]

4. Conclusion

This paper presents the microstructural characteristics of YSZ thin films deposited by spray pyrolysis. After deposition, YSZ thin films are amorphous with some 3 nm sized crystallites having a microstrain of 4%. During heating, the YSZ starts to crystallize; at 600 °C about 40% of the crystallization enthalpy is released and the crystallites have grown to a size of 5 nm with 1% microstrain. The material is fully crystalline at 900 °C or, after 17 h, at 600 °C . At this state, the grain size grew to 10 nm and the microstrain is reduced to at least 0.8%. The YSZ thin films consist of a mixture of cubic and the so-called t \bar{c} symmetry. The YSZ consists most probably of microdomains with t \bar{c} symmetry embedded in a cubic matrix. With increasing temperature or dwell time, the cubic content decreases. Simultaneously, the microstrain drops below 0.4%. The decrease in microstrain is correlated with increased tetragonal symmetry content. The cubic symmetry is favored in zirconia with high oxygen vacancy concentration (point defect concentration) and, therefore, high microstrain.^[69] It is thought that the t \bar{c} phase allows the YSZ crystals to relax.

Thin films exhibit different microstructures and crystallinity depending on the deposition and annealing conditions. Microstructure parameters such as the grain size, microstrain, and crystal symmetry as well as crystallinity are often not investigated in literature, but these structural changes may consequently influence the electrical properties. The various microstructures of the YSZ thin films deposited by spray pyrolysis may contribute to the explanation for the scatter in conductivity in literature.^[9–16] It is shown in this study that, depending on the annealing conditions, a YSZ spray pyrolysis film changes: i) from an amorphous to a fully crystalline microstructure, ii) its strain state from 4 to 0.4%, iii) its crystal symmetry from amorphous to mainly t \bar{c} with a significant Raman blue shift of up to 20 cm^{-1} wavenumbers for peak 4 and iv) its grain size from 3 to 130 nm. In order to capture the metastable phase and distorted lattice of these films, characterization further than conventional XRD analysis is required. It is advisable to vary just one microstructural parameter and investigate its influence on the electrical properties.

Additionally, the result that long term annealing at low temperature leads to full crystallization of thin films is very attractive for the future fabrication of MEMS devices. It means that gentle processing techniques at low temperature can be used which are suitable for MEMS processing.

Acknowledgements

The authors thank Anna Evans, Meike Schlupp, Thomas Ryll and Henning Galinski from the Nonmetallic Inorganic Materials of ETH Zurich (Switzerland) and Antonia Neels from the Microsystems Technology of CSEM in Neuchâtel (Switzerland) for stimulating discussions. The authors acknowledge support by the Electron Microscopy of ETH Zurich (EMEZ). Financial support by the following Swiss institutions is gratefully acknowledged:

- Center of Competence Energy and Mobility (CEEM) within the framework of the ONEBAT project
- Competence Centre for Materials Science and Technology (CCMX) within the framework of the NANCER project

- Swiss Electric Research (SER) within the framework of the ONEBAT project
- Swiss National Foundation (SNF) within the framework of the Sinergia project ONEBAT

Received: June 3, 2011

Published online: August 30, 2011

- [1] H. G. Scott, *J. Mater. Sci.* **1975**, *10*, 1527.
- [2] A. P. Caricato, A. Di Cristoforo, M. Fernández, G. Leggeri, A. Luches, G. Majni, M. Martino, P. Mengucci, *Appl. Surface Sci.* **2003**, *208–209*, 615.
- [3] P. Mengucci, G. Barucca, A. P. Caricato, A. Di Cristoforo, G. Leggeri, A. Luches, G. Majni, *Thin Solid Films* **2005**, *478*, 125.
- [4] R. Radhakrishnan, A. V. Virkar, S. C. Singhal, G. C. Dunham, O. A. Marina, *Sens. Actuators B* **2005**, *105*, 312.
- [5] A. Bieberle-Hütter, D. Beckel, A. Infortuna, U. P. Muecke, J. L. M. Rupp, L. J. Gauckler, S. Rey-Mermet, P. Mural, N. R. Bieri, N. Hotz, M. J. Stutz, D. Poulikakos, P. Heeb, P. Müller, A. Bernard, R. Gmür, T. Hocker, *J. Power Sources* **2008**, *177*, 123.
- [6] A. Evans, A. Bieberle-Hütter, J. L. M. Rupp, L. J. Gauckler, *J. Power Sources* **2009**, *194*, 119.
- [7] J. L. Hertz, A. Rothschild, H. L. Tuller, *J. Electroceram.* **2009**, *22*, 428.
- [8] B. Scherrer, A. Rossi, J. Martynczuk, M. D. Rossell, A. Bieberle-Hütter, J. L. M. Rupp, R. Erni, L. J. Gauckler, *J. Power Sources* **2011**, *196*, 7372.
- [9] I. Kosacki, T. Suzuki, V. Petrovsky, H. U. Anderson, *Solid State Ionics* **2000**, *136–137*, 1225.
- [10] D. Perednis, PhD Thesis, *Department of Materials*, Vol. 15190, Swiss Federal Institute of Technology Zurich, Zurich **2003**, *1*, 61.
- [11] T. Petrovsky, H. U. Anderson, V. Petrovsky, *Mater. Res. Soc. Symp. Proc.* **2003**, *756*, 515.
- [12] J. L. Hertz, H. L. Tuller, *J. Electroceramics* **2004**, *13*, 663.
- [13] J. H. Joo, G. M. Choi, *Solid State Ionics* **2006**, *177*, 1053.
- [14] M. F. Garcia-Sanchez, J. Pena, A. Ortiz, G. Santana, J. Fandino, M. Bizarro, F. Cruz-Gandarilla, J. C. Alonso, *Solid State Ionics* **2008**, *179*, 243.
- [15] S. Heiroth, T. Lippert, A. Wokaun, M. Dobeli, *Appl. Phys. A* **2008**, *93*, 639.
- [16] A. Infortuna, A. S. Harvey, L. J. Gauckler, *Adv. Funct. Mater.* **2008**, *18*, 127.
- [17] P. S. Patil, *Mater. Chem. Phys.* **1999**, *59*, 185.
- [18] D. Perednis, O. Wilhelm, S. E. Pratsinis, L. J. Gauckler, *Thin Solid Films* **2005**, *474*, 84.
- [19] C. Peters, A. Weber, B. Butz, D. Gerthsen, E. Ivers-Tiffée, *J. Am. Ceram. Soc.* **2009**, *92*, 2017.
- [20] C.-W. Kuo, Y.-H. Lee, I. M. Hung, M.-C. Wang, S.-B. Wen, K.-Z. Fung, C.-J. Shih, *J. Alloys Compd.* **2008**, *453*, 470.
- [21] S. Ramanathan, R. V. Muraleedharan, S. K. Roy, P. K. K. Nayar, *J. Am. Ceram. Soc.* **1995**, *78*, 429.
- [22] J. Málek, S. Matsuda, A. Watanabe, T. Ikegami, T. Mitsuhashi, *Thermochim. Acta* **1995**, *267*, 181.
- [23] P. Durán, J. Tartaj, J. F. Fernández, M. Villegas, C. Moure, *Ceram. Int.* **1999**, *25*, 125.
- [24] M. Yashima, M. Kakihana, M. Yoshimura, *Solid State Ionics* **1996**, *86–88*, 1131.
- [25] M. Yashima, K. Ohtake, M. Kakihana, H. Arashi, M. Yoshimura, *J. Phys. Chem. Solids* **1996**, *57*, 17.
- [26] B. Butz, H. Störmer, D. Gerthsen, C. Peters, A. Weber, E. Ivers-Tiffée, *Microsc. Microanal.* **2007**, *13*, 342.
- [27] W. Jung, J. L. Hertz, H. L. Tuller, *Acta Mater.* **2009**, *57*, 1399.
- [28] S. Heiroth, R. Frison, J. L. M. Rupp, T. Lippert, E. J. Barthazy Meier, E. Müller Gubler, M. Döbeli, K. Conder, A. Wokaun, L. J. Gauckler, *Solid State Ionics*, Submitted.
- [29] R. Neagu, E. Djurado, L. Ortega, T. Pagnier, *Solid State Ionics* **2006**, *177*, 1443.
- [30] J. Garcia-Barriocanal, A. Rivera-Calzada, M. Varela, Z. Sefrioui, E. Iborra, C. Leon, S. J. Pennycook, J. Santamaria, *Science* **2008**, *321*, 676.
- [31] C. Korte, A. Peters, J. Janek, D. Hesse, N. Zakharov, *Phys. Chem. Chem. Phys.* **2008**, *10*, 4623.
- [32] A. Karthikeyan, S. Ramanathan, *J. Applied Phys.* **2008**, *124314*, 4.
- [33] J. A. Kilner, *Nat. Mater.* **2008**, *7*, 838.
- [34] W. Araki, Y. Arai, *Solid State Ionics* **2010**, *181*, 1534.
- [35] A. Kushima, B. Yildiz, *J. Mater. Chem.* **2010**, *20*, 4809.
- [36] S. Ramanathan, *J. Vac. Sci. Technol. A* **2009**, *27*, 1126.
- [37] M. Sillassen, P. Eklund, N. Pryds, J. Bøttiger, *Solid State Ionics* **2010**, *181*, 864.
- [38] J. L. M. Rupp, A. Infortuna, L. J. Gauckler, *Acta Materialia* **2006**, *54*, 1721.
- [39] O. Wilhelm, S. E. Pratsinis, D. Perednis, L. J. Gauckler, *Thin Solid Films* **2005**, *479*, 121.
- [40] J. Rodríguez-Carvajal, *Physica B: Condensed Matter* **1993**, *192*, 55.
- [41] S. L. D. Lucato, *Department of Materials Science., Darmstadt University of Technology* **1998**.
- [42] B. Butz, H. Stormer, D. Gerthsen, M. Bockmeyer, R. Kruger, E. Ivers-Tiffée, M. Luysberg, *J. Am. Ceram. Soc.* **2008**, *91*, 2281.
- [43] K. T. Miller, C. J. Chan, M. G. Cain, F. F. Lange, *J. Mater. Res.* **1993**, *8*, 169.
- [44] H. E. Kissinger, *Anal. Chem.* **1957**, *29*, 1702.
- [45] M. M. R. Boutz, R. J. M. Olde Scholtenhuis, A. J. A. Winnubst, A. J. Burggraaf, *Mater. Res. Bull.* **1994**, *29*, 31.
- [46] J. Li Vage, K. Doi, C. Mazieres, *J. Am. Ceram. Soc.* **1968**, *51*, 349.
- [47] J. L. M. Rupp, B. Scherrer, L. J. Gauckler, *Phys. Chem. Chem. Phys.* **2010**, *12*, 11114.
- [48] K. Nishizawa, T. Miki, K. Suzuki, K. Kato, *Thin Solid Films* **2007**, *515*, 4004.
- [49] H. H. Huang, C. C. Diao, C. F. Yang, C. J. Huang, *J. Alloys Compd.* **2010**, *500*, 82.
- [50] A. Feinberg, C. H. Perry, *J. Phys. Chem. Solids* **1981**, *42*, 513.
- [51] T. Merle, R. Guinebreteiere, A. Mirgorodsky, P. Quintard, *Phys. Rev. B* **2002**, *65*, 144302.
- [52] G. Fadda, G. Zanzotto, L. Colombo, *Phys. Rev. B* **2010**, *82*, 064106.
- [53] P. Bouvier, G. Lucazeau, *J. of Phys. Chem. of Solids* **2000**, *61*, 569.
- [54] A. Kuwabara, T. Tohei, T. Yamamoto, I. Tanaka, *Phys. Rev. B* **2005**, *71*, 064301.
- [55] F. Capel, M. A. Bañares, C. Moure, P. Durán, *Mater. Lett.* **1999**, *38*, 331.
- [56] M. Ishigame, E. Yoshida, *Solid State Ionics* **1987**, *23*, 211.
- [57] R. Krishnamurthy, Y. G. Yoon, D. J. Srolovitz, R. Car, *J. Am. Ceram. Soc.* **2004**, *87*, 1821.
- [58] S. Shin, M. Ishigame, *Phys. Rev. B* **1986**, *34*, 8875.
- [59] F. F. Lange, *Science* **1996**, *273*, 903.
- [60] M. E. Manriquez, M. Picquart, X. Bokhimi, T. Lopez, P. Quintana, J. M. Coronado, *J. Nanosci. Nanotechnol.* **2008**, *8*, 6623.
- [61] M. A. Blesa, A. J. G. Maroto, S. I. Passaggio, N. E. Figliolia, G. Rigotti, *J. Mater. Sci.* **1985**, *20*, 4601.
- [62] P. D. L. Mercera, J. G. Van Ommen, E. B. M. Doesburg, A. J. Burggraaf, J. R. H. Ross, *J. Mater. Sci.* **1992**, *27*, 4890.
- [63] K. S. Mazdiyasn, C. T. Lynch, J. S. Smith, *J. Am. Ceram. Soc.* **1966**, *49*, 286.
- [64] J. P. Goff, W. Hayes, S. Hull, M. T. Hutchings, K. N. Clausen, *Phys. Rev. B* **1999**, *59*, 14202.
- [65] B. Butz, P. Kruse, H. Störmer, D. Gerthsen, A. Müller, A. Weber, E. Ivers-Tiffée, *Solid State Ionics* **2006**, *177*, 3275.
- [66] B. Butz, R. Schneider, D. Gerthsen, M. Schowalter, A. Rosenauer, *Acta Mater.* **2009**, *57*, 5480.
- [67] J. G. Allpress, H. J. Rossell, *J. Solid State Chem.* **1975**, *15*, 68.
- [68] H. J. Rossell, J. R. Sellar, I. J. Wilson, *Acta Cryst. B* **1991**, *47*, 862.
- [69] F. Zhang, P. J. Chupas, S. L. A. Lui, J. C. Hanson, W. A. Caliebe, P. L. Lee, S.-W. Chan, *Chem. Mater.* **2007**, *19*, 3118.